Chapter 6

Magnetic Materials by Melt Spinning Method, Structural Characterization, and Numerical Modeling

Marcelo Rubén Pagnola, Jairo Useche Vivero and Andrés G. Marrugo

Additional information is available at the end of the chapter

http://dx.doi.org/10.5772/intechopen.77368

Abstract

Chill block melt spinning is used in industrial processes for the production of metallic glasses. It is a rapid solidification process whereby a liquid metal is ejected at high pressure and temperature via a nozzle onto a rotating wheel solidifying in the form of a ribbon. In this work, starting from an alloy with the composition of $Fe_{78}Si_9B_{13}$ (% at.) reproduces the melt spinning technique to get the amorphous magnetic material. A *CFD3D* model based on the finite volume method (*FVM*) is proposed. For this purpose, the *OpenFoam*® open source code is used. In the ribbon production stage, it has been observed that the turbulence involved in the first reported transient lasts a few milliseconds, enough time to study the process with high-speed cameras. We measure the ejection speed by using optical flow on the melt contour. This enables us to check defects in the ribbons, which are predicted with the computational model, such as the case of cracks caused by irregularities in the first formation of the solid layer. The temperature measurement method relies on the fact that the digital camera is sensitive to electromagnetic radiation between 400 and 1000 nm in wavelength and the fact that the image gray level, which is proportional to the temperature *T*, provided the background illumination level is negligible.

Keywords: melt spinning, magnetic materials, OpenFoam, CFD, finite volume method

1. Introduction

Since the 1980s, the production of magnetic materials has been carried out mainly through the melt spinning process. These materials, obtained in the form of low thickness ribbons, have increased magnetic capacities with the utilization of alloys with amorphization capacity and

nanocrystalline. Among these alloys, those of $Fe_{78}B_{13}Si_9$ (% at.) for electric transformer cores are the most used because they manage to reduce vacuum losses up to 80% when compared to those of the cores constructed with oriented grain *FeSi* sheets, normally used in these devices. The melt spinning process consists of forming a thin sheet of metal alloy on a rotating flat surface at a constant temperature. In this process, a jet of liquid metal is expelled through a nozzle by the overpressure of an inert gas, and it impacts on the surface of a rotating solid copper wheel. In this way, it forms a thin layer of molten material that quickly solidifies as a continuous ribbon that is then collected and rolled to obtain the magnetic coils as the final product. According to the distance between the nozzle and the rotating wheel (gap), the following processes are determined: *chill block melt spinning* (*CBMS*) and *planar flow casting* (*PFC*). In the *CBMS*, the jet of liquid metal is expelled through a nozzle with a gap >1 mm. In the *PFC*, however, the gap is less than 1 mm. In these sections, we will talk about the production of amorphous magnetic ribbons and the numerical modeling of the shaping process and its control of variables through the capture of high-resolution images.

2. Materials and methods

2.1. Set-up and production

$Fe_{78}Si_9B_{13}$ (% at.) ribbons are produced from an initial ingot previously melted in a vacuum atmosphere and a graphite crucible, from noncommercial alloys. The impurities in the noncommercial alloy are *Al*, *C*, *Ca*, and *S*. Their quantity is lower than 0.3% wt. These ribbons were cooled on the copper wheel with temperature controlled by optical pyrometer on a tripod located at 1 m of focal distance from the melted sample [1, 2].

These operations are developed in a 7.5 kW induction furnace *RDO*™ model *LFI-7.5* mounted as shown in **Figure 1**. The arrangement is formed by an induction coil inside a vacuum chamber, where an inert atmosphere is produced previously with a mechanical vacuum pump. The gap values used are typical to identify this methodology as chill block melt spinning [3].

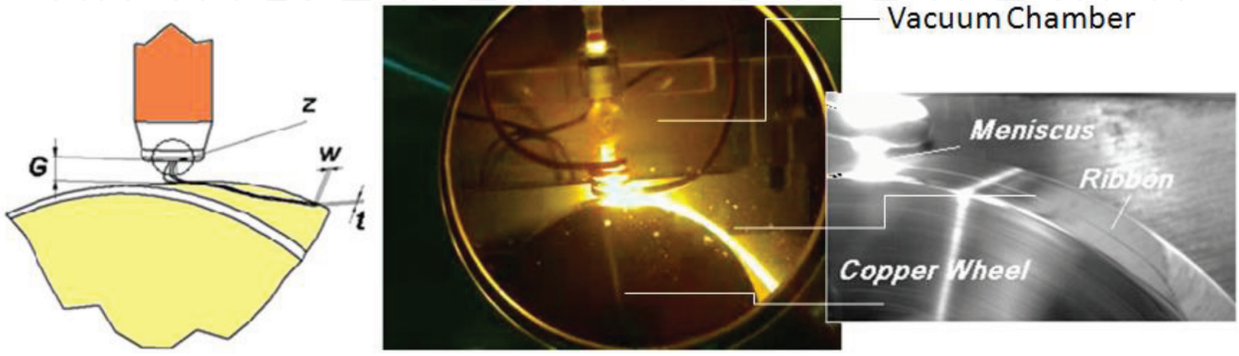

Figure 1. Melt spinning equipment and process of $Fe_{78}B_{13}Si_9$ (% at.) ribbons.

http://dx.doi.org/10.5772/intechopen.77368

With an argon overpressure, the alloy melted is expulsed through the nozzle at an ejection velocity over the spinning wheel. Our implementation of the process captured with a high-speed camera can be observed in **Figure 2(a)**. It is similar to the one reported by Ames Laboratory, USA in **Figure 2(b)**.

To determine the width (w), we used a vernier with 0.02 mm precision and an external micrometer (0–25 mm) with 0.01 mm precision for thickness (t) determination. Three sections of approximately 100 mm of each ribbon were selected in five measurement places. An average value was reported.

2.2. Obtained product and results

The cooling rate was estimated according to -2.73×10^6 K/s with a wheel speed (V_x) in accordance with **Table 1**, and the relationship $x/z = 3.8395$, being $z = 0.0006$ m the orifice diameter in the nozzle with a solidification time of 9.4×10^{-7} s [4].

In **Figure 3**, the z/w ratio decay for the measured values with gaps (G) 2, 3, and 4 mm and orifice diameter (z) of 0.7 mm is shown. Between 35 and 40 m/s in the 2 mm gap curve, microspheres were obtained without ribbon formation, due to speeds of over 30 m/s, local vortices appear in the surrounding atmosphere that increases the convective flow along the wheel surface. These values define the vorticity in the contact zone, showing the influence of the coefficient of convective heat transfer (h) and the Biot number (B_i) as shown in **Figure 4**.

This effect is indicative of the Newtonian cooling in the solidification process of amorphous ribbons. The features are already reported by Pagnola et al. [4, 5]. For wheel speeds between 5 and 40 m/s, the thickness (t) values are compared with Tkatch et al. [6] and are plotted in **Figure 5**.

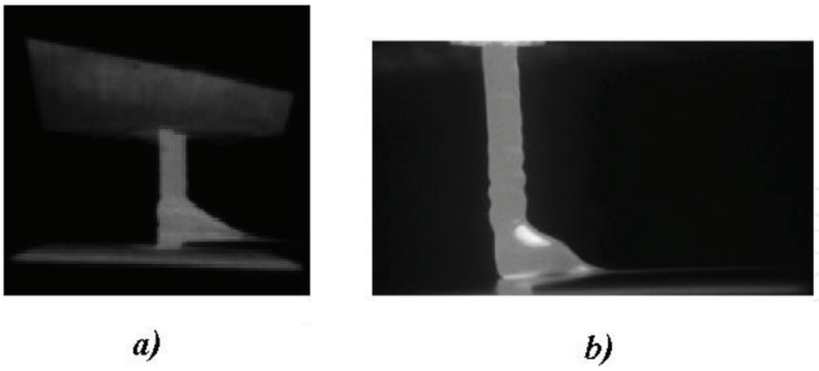

Figure 2. (a) *CBMS* of $Fe_{78}B_{13}Si_9$ (% at.) in *Pilot Plant of Magnetics Materials* (*INTECIN*) in **Table 1** conditions. (b) Similar *CBMS* process courtesy of *Ames Lab, US DOE*.

Speed wheel (m/s)	Gap (mm)	Ejection pressure (bar)
5–40	2, 3, and 4	0.3

Table 1. Production parameters.

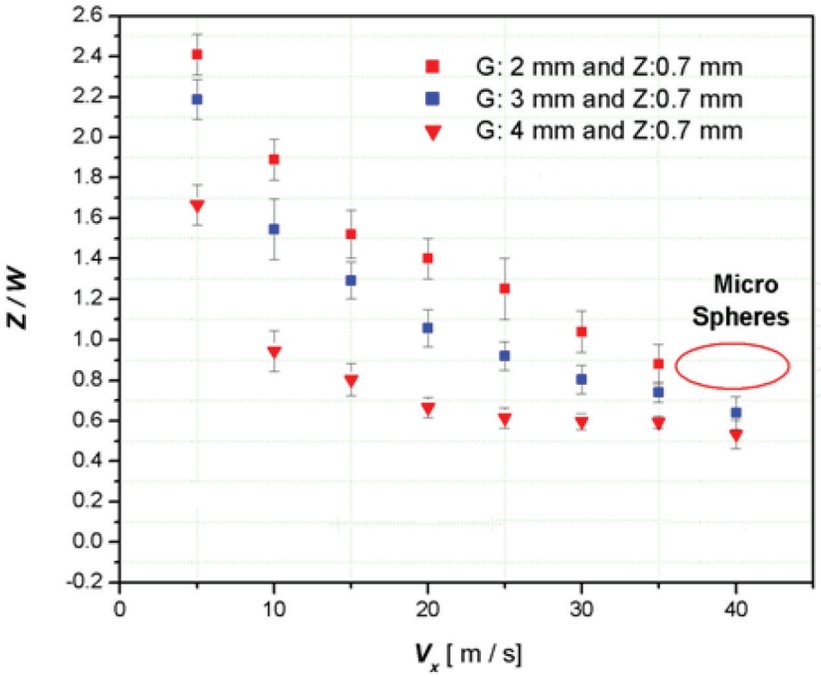

Figure 3. Comparative decreasing of *z/w* ratio with the tangential velocity *Vx*.

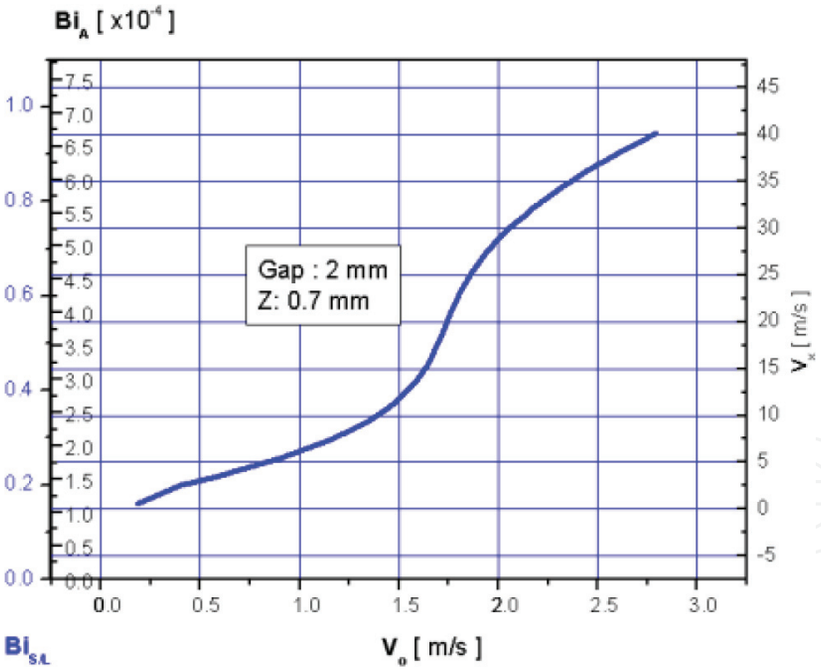

Figure 4. Triple entrance curve for the velocity values in the nozzle (V_0) that determine the Biot number according to the speed of the wheel *Vx* for *G* = 2 and *Z* = 0.7 mm.

The turbulence involved in the reported solidification times lasts a few milliseconds. Enough time to study the process with high-speed cameras and recreate *3D* numerical simulations that originate the defects that appear in the conformation of the ribbon is as follows:

http://dx.doi.org/10.5772/intechopen.77368

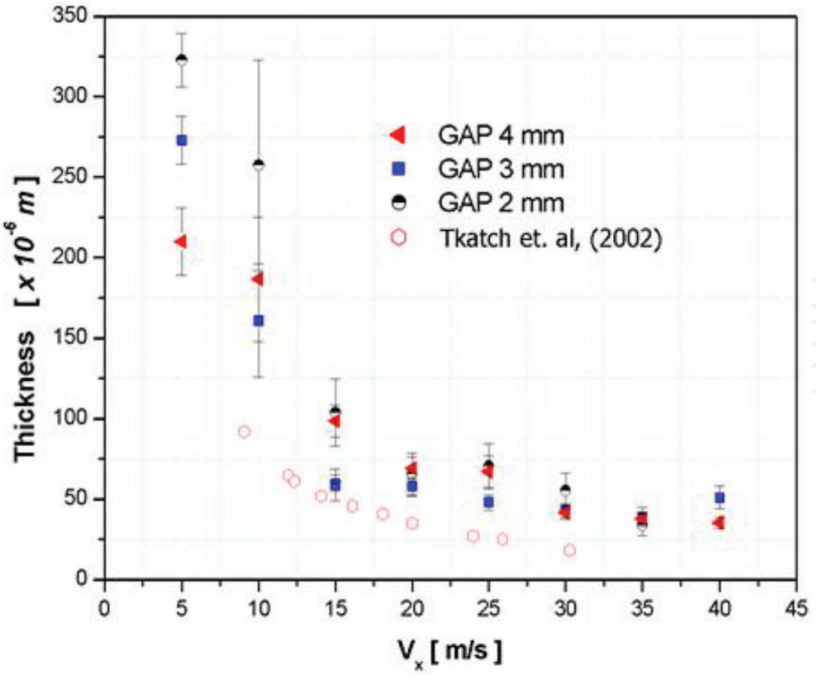

Figure 5. Comparative decreasing of ribbon thickness (t) with V_x.

Defects in the solidification: At the beginning of the ejection, the formation of a meniscus of material generates an irregular profile with changes in the ribbon thickness, which is still in a liquid state. The contact of this irregular thickness profile makes the solidification process begin in the thinnest part of the film because this is the one that changes its temperature faster and, therefore, its viscosity. This mechanism causes a continuous solid contour similar to that of a hole to be generated, which propagates in the film while continuing to maintain that thin thickness (*Point 1*—**Figure 6**).

Transition zone: It appears in a more stable meniscus, and subsequently, some are observed irregularities. This zone has a constant contour, and the ribbon with almost imperceptible defects of the order of 5 μm can be observed (*Point 2*—**Figure 6**).

Zone of homogeneous thickness: Once the turbulence in the meniscus is over after which the process stabilizes, the defects disappear giving way to a continuous ribbon with properties and qualities ready for specific use in electronic devices and with qualities that far exceed standard materials, such as its frequency response to variable magnetic fields. The scanning electron microscopy (*SEM*) view (*Point 3*—**Figure 6**) is consistent with the expectation of an achieved high cooling rate that avoids the total crystallization, resulting in an amorphous structure confirmed by X-ray diffraction (*XRD*) and Mössbauer Microscopy (*MS*) analysis. Similar to the report by Miglierini [7], it can be attributed to *Fe* atoms surrounded by *Si* atoms, in a remanent amorphous phase attributed to *FeB* environments, according to Franke et al. [8], and environments rich in *Si* [4]. The difficulty of analyzing with the transmission electron microscopy (*TEM*) is due to the obtained average thickness of the ribbons because their commended thickness is limited to few hundreds of nanometers in this technique [9]. Later isothermal annealing on these tapes at temperatures close to 700°C indicates predominantly the formation of *nanocrystalline*

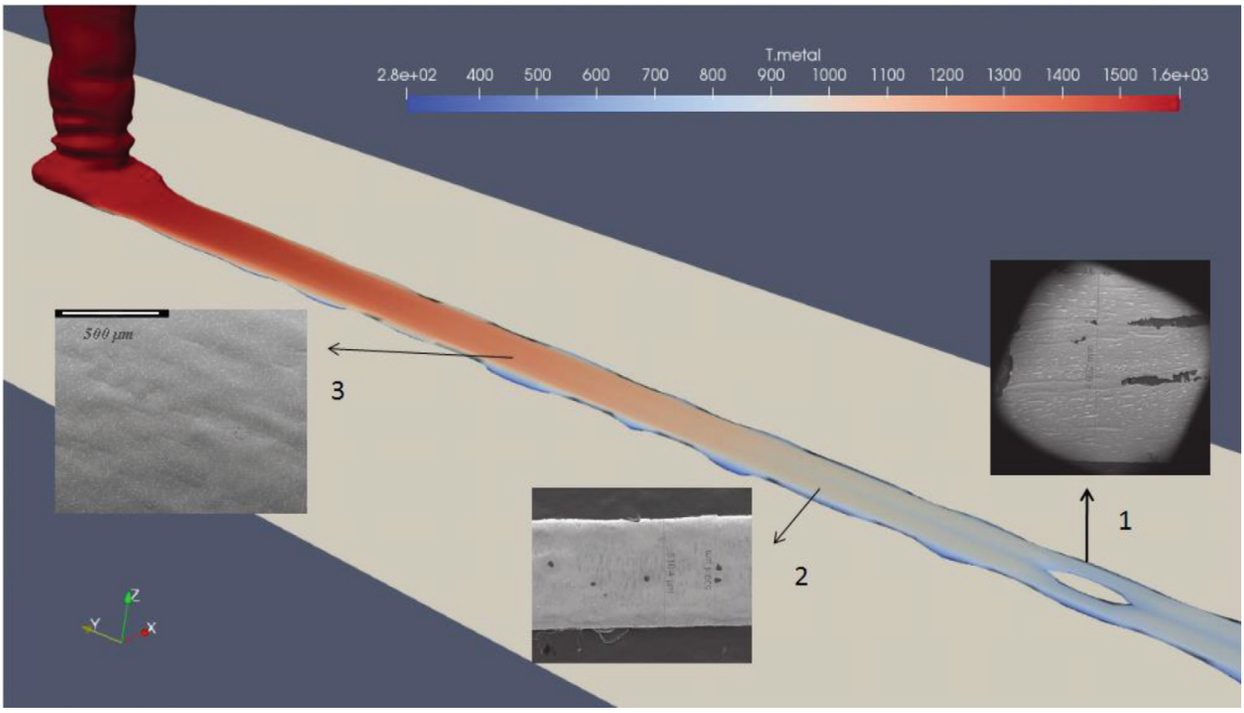

Figure 6. Characteristic zones of the production process.

structures with sizes that reach 6.31 nm over phases such as *FeB* [4]. Another way to obtain nanostructures is by isothermal annealing of melt-spun ribbons at 823 K for 1 h with the replacement of *B* for *Ge*: $Fe_{73.5}Si_{13.5}$ $Ge_2B_7Nb_3Cu_1$ and $Fe_{73.5}Si_{13.5}Ge_4B_5Nb_3Cu_1$ [10].

The Vickers microhardness *HV 0.05* was determined in an average of a total of 10 measurements (**Figure 7**), obtaining a hardness of *1070 HV0.05*, equivalent to approximately *70 HRC, Rockwell C* scale.

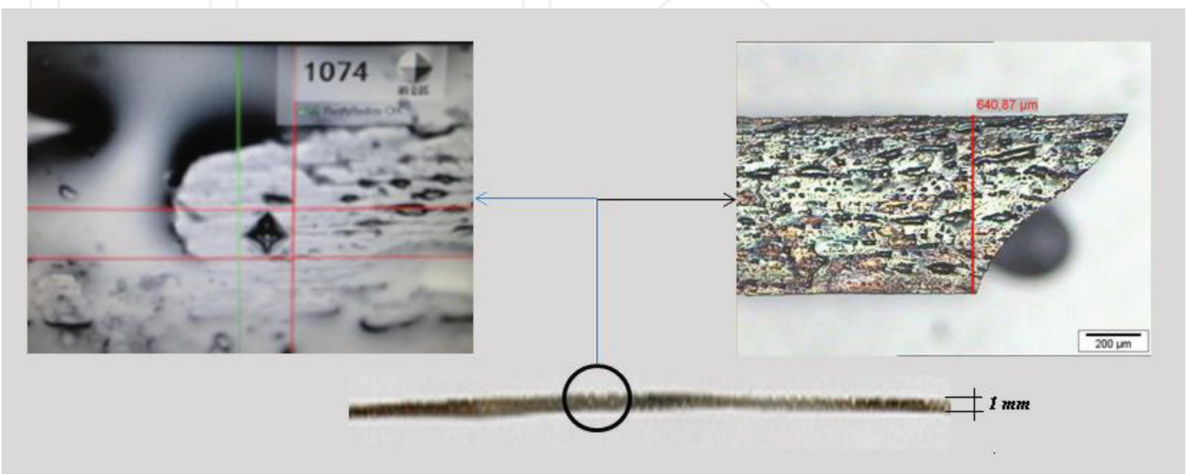

Figure 7. $Fe_{78}B_{13}Si_9$ (% at.) obtained ribbon.

http://dx.doi.org/10.5772/intechopen.77368

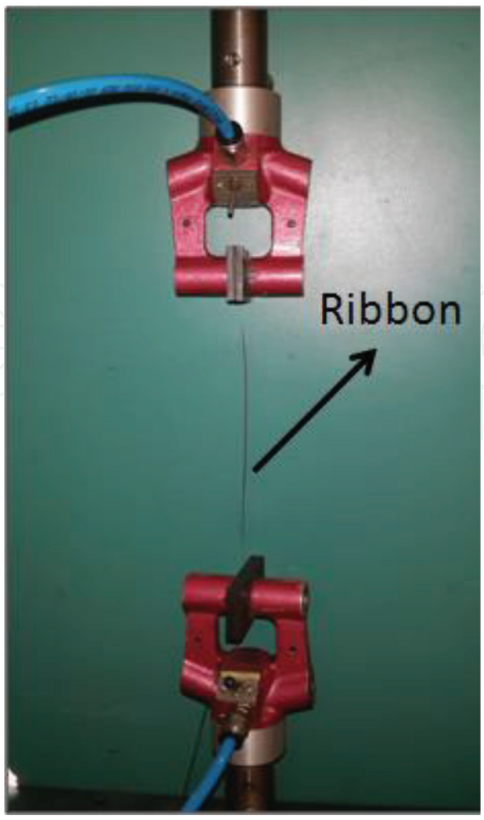

Figure 8. Tensile test on $Fe_{78}B_{13}Si_9$ ribbons.

Sample	n
Breakage average load (N)	11.95
Average section (mm^2)	0.063
Average resistance to traction (MPa)	190

Table 2. Average results of tensile tests on $Fe_{78}B_{13}Si_9$ ribbons.

For the tensile test of the ribbons, the device of **Figure 8** was used. Average values in 10 different samples were determined in **Table 2**.

3. Computational modeling

The work of Bussmann et al. [11] proposes a numerical solution of the equations of momentum and energy to study the condition of stable flow and temperature field in the puddle of the process of melt spinning. The proposed model considers the inertial effects, viscous, the surface tension, and the dependence of the viscosity with the temperature until the solidification of the material to an amorphous state.

In the work of Babei et al. [12], a numerical formulation based on the finite difference method is proposed to model the flow and heat transfer phenomenon transient in melting process. The results are contrasted with experimental models finding high consistency between the results.

In the work of Hui et al. [13], a numerical model is proposed for the study of the process of heat transfer and transient flow in the melt spinning process using the Navier-Stokes equations and the heat transfer equation. The proposed model allows the calculation of the cooling speeds along the thickness of puddle for different wheel speeds. Using experimental models, temperature distributions and cooling velocities were obtained, and similar results to those found in the numerical model were obtained.

Wang and Matthys [14] present a bi-dimensional finite difference semi-implicit numerical model for the study of the flow field and heat transfer with phase change in the casting model process. The boundary-layer theory is used to model these fields during the solidification process of the puddle.

Steen and Karcher [15] present the analysis of casting metals using spinning wheels. This work presents a broad discussion of flow stability, a relevant aspect in non-stable flow phenomena, which influences the movement of the meniscus, final texture, and instability of the morphological type of the solidification front.

Theisen et al. [16] focus their study on the behavior of the melt spinning process in time. The model developed is based on the equations of mass balance in unstable state combined with the Bernoulli equation of the flow. The proposed model allows to establish variations in different time scales, allowing to determine the time scale in which the process can be considered as stable. The evolution of the length of the puddle and the thickness of the produced metal tape indicates that the solidification speed varies over time.

In the work of Sowjanya and Kishen Kumar Reddy [17], they investigate the flow field of molten material in the puddle by determining pressure profiles, flow lines, and current function according to the injection pressure of the material in the nozzle. The proposed model allows to determine the point of separation of the material of the wheel to form the tape.

Sowjanya and Kishen Kumar Reddy [18] propose a bi-dimensional numerical model to model the molten puddle during the melt spinning process by finding stable puddle formation times related to its injection pressure. The comparison of experimental thicknesses with numerical results has a high concordance.

3.1. Governing equations

The numerical model is based on the following assumptions [11]:

- The width of the tape is much greater than the height of the gap, then puddle is considered essentially two dimensional.
- As the diameter of the wheel is much greater than the length of the puddle, the curvature of the wheel beyond the puddle is negligible. In addition, the lower surface of the puddle is considered flat.

- Molten material and the fluid that surrounds the puddle are considered as incompressible and a Newtonian fluid with laminar behavior.
- Density, surface tension, and thermal diffusivity of the molten material are considered constant. Kinematic viscosity depends on temperature.
- The heat flow between the tape and the wheel is of the convective type. The temperature of the wheel remains constant. The transfer of heat by radiation from the puddle is negligible.

The basic equations that govern the phenomenon of molten metal flow in the melt spinning process are given by the mass balance equation:

$$\nabla . v = 0 \tag{1}$$

where v is the velocity field. The equation of momentum balance for a Newtonian fluid is given by:

$$\rho \frac{Dv}{Dt} = -\nabla p + \eta \Delta v + \rho b \tag{2}$$

where ρ is the density of the fluid; p is the pressure field; η is the kinematic viscosity; and b is the vector of mass forces. The energy conservation equation:

$$\rho c_p \frac{DT}{Dt} = -\nabla . (\lambda \nabla T) + \eta \acute{\gamma} 2 + \acute{q}_{LH} \tag{3}$$

where c_p is the specific calorific capacity of molten material; T specifies the temperature field value; λ is the thermal conductivity of the fluid; $\acute{\gamma}$ represents the rate of deformation; and $\acute{q}_{LH}$ is the latent heat flux. The transportation equation that controls the movement of the free surface is given by:

$$\frac{\partial \Phi}{\partial t} + \nabla . (\Phi v) = \frac{D\Phi}{Dt} + \Phi . (\nabla . v) = 0 \tag{4}$$

In this equation, $\Phi(x)$ is the volume of fluid function (*VOF*), which is a discontinuous function that measures the amount of fluid present in a volume element taking values between 0 and 1 ($\Phi(x) = 0$, if the volume of fluid does not contain molten material and $\Phi(x) = 1$, when the volume contains entirety molten material).

3.2. Boundary conditions

On the solid surfaces of the injection and wheel nozzle, a non-slip and non-penetration flow condition is considered. On the surface of the wheel, the fluid moves at the same speed as the wheel. The *VOF* model is used through the transport equation to model the puddle-air interface. On the free surface of the inlet nozzle, a known pressure condition is used, which is equal to the injection pressure condition of the molten metal. As we have explained in [19], the flow of heat between the puddle and the wheel is modeled by:

$$\lambda \nabla T = h(T_{int} - T_{\infty}) \tag{5}$$

where h is the convective coefficient; T_{int} is the temperature at molten material on the wheel; and T_{∞} is the room temperature [20].

4. Image-based measurements

CBMS is a highly sensitive process in which many variables should be taken into account both for computational modeling purposes and for quality control. To monitor the ribbon production stage and to validate our proposed model, we carried out several experiments via high-speed image acquisition using a *Vision research Phantom-HD* [21]. Using a high-speed camera, we can accurately determine the ejection speed and the temperature of the molten alloy as it flows from the nozzle to the spinning wheel. In the following subsections, we explain the image-based measurement details.

4.1. Ejection velocity measurement

The most frequently used technique for studying the *2D* and *3D* velocity field of fluids is called *particle image velocimetry* (*PIV*) [22]. It is an optical method of flow visualization in which the fluid is seeded with small tracer particles, assumed to follow the flow dynamics, and illuminated so that the particles are visible. The motion of the seeding particles is used to calculate the velocity field of the flow. However, to use *PIV*, the fluid has to be transparent and at temperatures that typically do not exceed 200°C [23]. In our case, *PIV* is not readily an option because the considered molten alloy in the melt spinning process is not transparent, and seeding a fluid at temperatures above 1000°C is not possible. Therefore, we limit our analysis to the measurement of the ejection velocity.

The ejection velocity of the molten alloy is a parameter that is directly linked to the ejection pressure, the fluid viscosity and temperature, and nozzle size. This velocity can be measured using image-based velocimetry. Recently, image-based velocimetry has become more attractive than *PIV* because of the advancement in computing power [24]. The most used image-based technique for estimating *2D/3D* motion or velocity fields is optical flow. Optical flow methods try to calculate the motion between the two image frames acquired at times t and $t + \Delta t$ at every pixel position. For a *2D* + *t* dimensional case, the assumption is that a pixel at location (x, y, t) with an intensity $I(x, y, t)$ will have moved by Δx, Δy, and Δt between the two image frames. This assumption is called the brightness constancy constraint and is given by the following expression [25]:

$$I(x, y, t) = I(x + \Delta x, y + \Delta y, t + \Delta t) \tag{6}$$

On the assumption that the movement is small, the image constraint at $I(x, y, t)$ can be expanded with a Taylor series to get

http://dx.doi.org/10.5772/intechopen.77368

$$I(x+\Delta x, y+\Delta y, t+\Delta t) = I(x,y,t) + \frac{\partial I}{\partial x}\Delta x + \frac{\partial I}{\partial y}\Delta y + \frac{\partial I}{\partial t}\Delta t + H.O.T. \tag{7}$$

From these equations, it follows that

$$\frac{\partial I}{\partial x}V_x + \frac{\partial I}{\partial y}V_y + \frac{\partial I}{\partial t} = 0 \tag{8}$$

where V_x and V_y are the x and y components of the velocity or optical flow of $I(x,y,t)$, and $\frac{\partial I}{\partial x}$, $\frac{\partial I}{\partial y}$, and $\frac{\partial I}{\partial t}$ are the derivatives of the image at (x,y,t) in the corresponding directions. Eq. (8) has two unknowns and cannot be solved without additional equations or constraints. All optical flow methods introduce additional conditions for estimating the actual flow. In this work, we use the Lucas-Kanade method [26] in which the underlying assumption is that the flow is essentially constant in a local neighborhood of the pixel under consideration. Therefore, the optical flow equations for all the pixels in a given neighborhood are solved in the least-square sense.Using optical flow, we can compute the two components (u,v) of velocity per pixel. However, often such high-resolution optical flow is not needed, and at that resolution, the resulting flow is noise prone. In our implementation, the optical flow estimation uses median filtering to obtain a noise robust *2D* velocity field from which we can obtain the ejection velocity. In addition, we obtain a binary mask to compute the optical flow from the region of interest to avoid detecting changes in brightness or reflections on the wheel as motion. In **Figure 9**, we show the successive image frames during ejection for a single experiment. The first frame shows the crucible, and the nozzle before the ejection, the intermediate frames show the ejection of the molten alloy, and the final frame shows the instant when the alloy comes into contact with the spinning wheel and starts to flow. From these data, we can calculate many parameters related to the ejection. We show the maximum speed per frame. At a frame rate of 5602 fps, the molten alloy takes about 14 frames to be ejected and comes into contact with the rotating wheel. Knowing the gap between the nozzle and the wheel (2 mm) and the fact that the alloy takes 2.499 ms to come into contact with the wheel, we compute an average speed of 0.80 m/s (**Figure 2**). This value is in agreement with the computed maximum speeds as shown in **Figure 9**.

4.2. Temperature measurement

CBMS is a technological process characterized by high-material velocities in which a precise high-speed temperature measurement is essential. Due to the presence of multiple flow phases and the high temperatures of the molten alloy (often above 1500°C), only non-contact methods can be used to measure the temperature. Pyrometers and infrared cameras are the most common non-contact temperature measurement devices [27]. However, on the one hand, pyrometers are only capable of single-point temperature measurements. On the other hand, despite the high cost, infrared cameras are not appropriate for high-speed applications due to their limited spatial resolution and dynamic response.The ejected molten alloy in the melt spinning process can reach temperatures well above 1500°C. At this temperature, the alloy emits a considerable amount of light in the visible and near infrared part of the electromagnetic spectrum. Roughly between

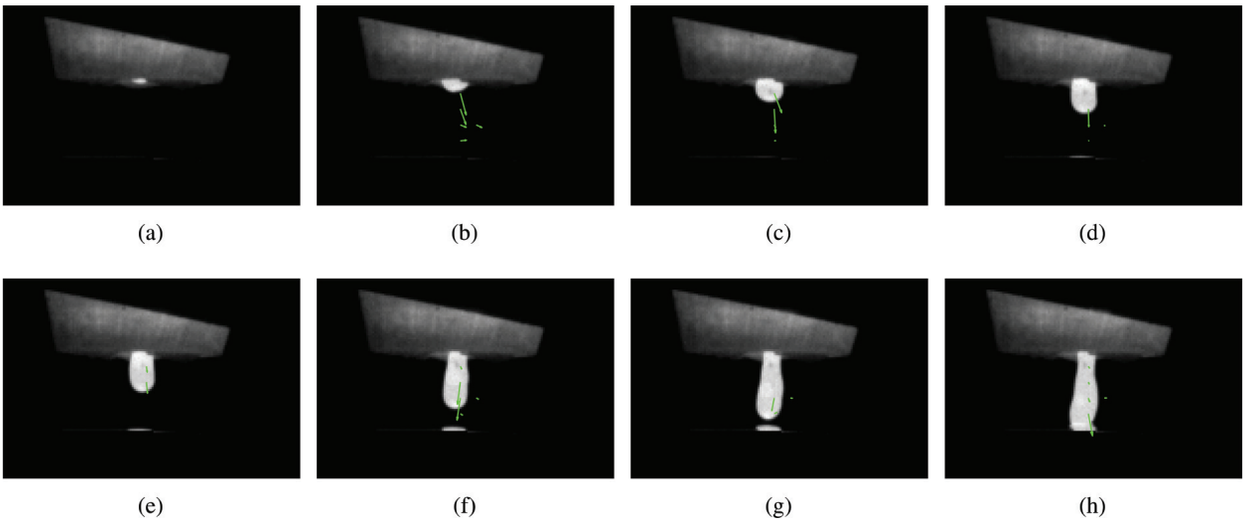

Figure 9. Velocity measurement of molten alloy ejection by optical flow. The arrows indicate the most significant velocity. Maximum speed: (a) 0.008 m/s; (b) 0.087 m/s; (c) 0.408 m/s; (d) 1.227 m/s; (e) 1.354 m/s; (f) 1.193 m/s; (g) 0.745 m/s; and (h) 0.806 m/s.

400 nm and 1000 nm, this band is where standard *CCD* and *CMOS* camera sensors are most sensitive. This advantage is the reason for using conventional high-speed imaging cameras for temperature measurement.In our *CBMS* experimental set-up, we measured the temperature of the molten alloy using the recently proposed method by Bizjan et al. [28]. Using a high-speed monochrome camera, we capture intensity images in 10-bit resolution and size 320 × 200 at 5602 fps. For the temperature calculation, the required input is the normalized image gray level G, 0 (black) ≤ G ≤ 1 (white). This gray level is assumed to be proportional to the camera sensor voltage response due to the incident light, which in turn depends on the equations for gray body radiation. The equations for calculating the temperature are as follows:

$$T_k = C^4 \sqrt{\frac{G}{k \cdot \eta(T_k) \cdot t_E \cdot \sigma_s}} \tag{9}$$

$$\eta = \frac{\int_0^\infty Y(\lambda) B_\lambda(\lambda) d\lambda}{\int_0^\infty B_\lambda(\lambda) d\lambda} \approx \frac{\sum_{0.4\ \mu m}^{1 \mu m} Y(\lambda) B_\lambda(\lambda) \Delta\lambda}{\frac{2}{15} \frac{\pi^4 k_B^4}{h^3 c^2}} \tag{10}$$

$$B_\lambda = \frac{2hc^2}{\lambda^5} \frac{1}{\exp\left(hc/\lambda k_B T_K\right) - 1} \tag{11}$$

In Eqs. (9)–(11), T_K is the absolute temperature in (K); k is the camera sensor sensitivity; t_E is the camera shutter time; η is the light efficacy; Y is the sensor quantum efficiency; λ is the wavelength of light; and B_λ is the spectral radiance. The physical constants are σ_s = 5.67 × 10^{-8} W m^{-2} K^{-4} (Stefan-Boltzmann constant); k_B = 1.381 × 10^{-23} J/K (Boltzmann constant); h = 6.626 × 10^{-34} J s (Planck constant); and c = 2.998 × 10^8 m/s (speed of light in vacuum).

As proposed by Bizjan et al. [28], many variables are not directly measured or known, but it is safe to assume that they remain constant during the experiment. The constant C implicitly contains all these variables, and its value depends on the measurement set-up. These variables

http://dx.doi.org/10.5772/intechopen.77368

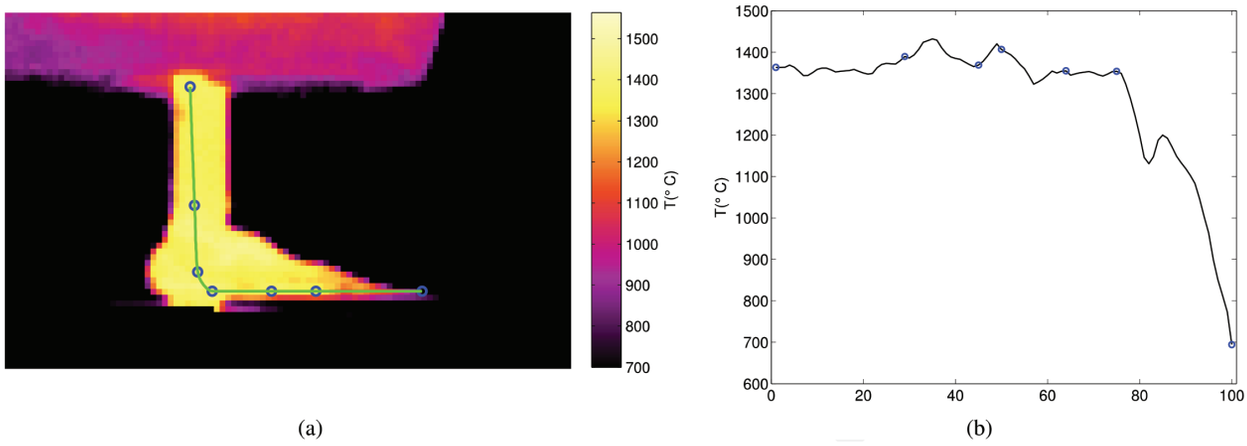

Figure 10. Temperature measurement by high-speed camera.

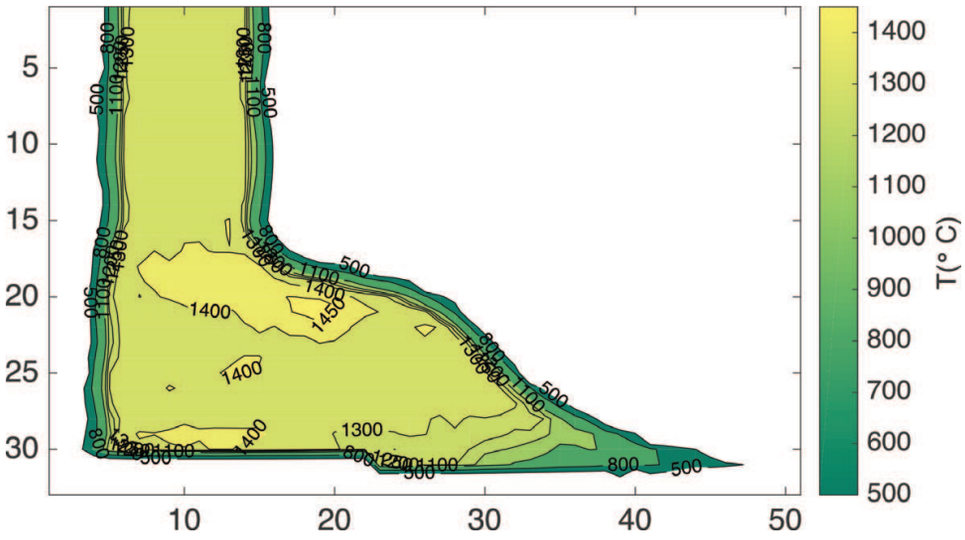

Figure 11. Temperature field as a contour plot.

include the surface emissivity e (proportional to C^4), the lens aperture setting, the focal distance, and the internal light absorption. The constant C is obtained from Eq. (6) by means of calibration to a surface with a known reference temperature and the corresponding image gray level at that location. In our experiments, we measured the reference temperature with a pyrometer.

In **Figure 10**, we show the stable flow of the molten alloy in the *CBMS* process. The green profile indicates the rapid cooling rate with a drop from approximately 1300 to 400°C in a distance of less than 1 mm. To accurately assess the beginning of the solidification process, we show in **Figure 11** the temperature flow field as a contour plot and note the lower regions with temperatures below 800°C.

5. Conclusions

In this chapter, we have described the *CBMS* industrial process for a commercial alloy of $Fe_{78}Si_9B_{13}$ (% at.) used in the industry as a magnetic material for applications in the electrical

transformer industry. We have studied this practical process from the generation of a mother alloy to its casting into a thin ribbon for its industrial application. The production parameters corresponding to its ejection have been reported under different conditions and compared with those obtained by other authors, resulting in similar characteristics in both thickness (*t*) and width (*W*). The mechanical parameters of the produced ribbons are reported. In addition, we have described the turbulence phenomena reported in previous works. This turbulence was introduced in the numerical modeling with the *FVM* methodology, agreeing with defects found in the rugosity of the ribbon in different areas perfectly differentiated characteristics in the solidification process (see **Figure 6**). In the computational modeling of the process, we provide a brief review of other numerical methodologies used by different authors and the equations that govern the phenomenon along with the boundary conditions used in the numerical simulation procedure. We describe the most critical process for the considered parameters. In addition, we showed different methodologies for the digital capture of data to compare the temperature and velocity profiles obtained in the process that allow validating the temperature profiles obtained in the numerical simulations to obtain the solidification profiles in the finished product.

Acknowledgements

The three authors of this chapter, *MRP*, *JUV,* and *AGM*, are grateful to the projects *UBACyT 20020150100088BA*; *PDTS-CIN 0362*. This work was supported by *CONICET*; University of Buenos Aires; and *COLCIENCIAS*.

Conflict of interest

It is hereby acknowledged that all the authors participating in this work do not present any real or potential conflict of interest, including financial aspects.

Author details

Marcelo Rubén Pagnola[1]*, Jairo Useche Vivero[2] and Andrés G. Marrugo[2]

*Address all correspondence to: mpagnola@fi.uba.ar

1 University of Buenos Aires, National Council of Scientific and Technical Research, Institute of Technology and Engineering Sciences "Ing. Hilario Fernández Long" (INTECIN), Buenos Aires, Argentine

2 Facultad de Ingeniería, Universidad Tecnológica de Bolívar, Cartagena, Colombia

References

[1] Pagnola M, Saccone F, Ozols A, Sirkin H. Improvement to approximation of second order function of hysteresis in magnetic materials. COMPEL: The International Journal for Computation and Mathematics in Electrical and Electronic Engineering. 2009;**28**(6):1579-1589. DOI: 10.1108/03321640910999879

[2] Pagnola M, Katabian R. Development of a winding mechanism for amorphous ribbon used in transformer cores. In: Gokcek M, editor. Mechanical Engineering. Rijeka: InTech; 2012. pp. 277-291. DOI: 10.5772/37331. ISBN: 978-953-51-0505-3, Chapter 12

[3] Pavuna D. Production of metallic glass ribbons by the chill-block melt spinning technique in stabilized laboratory conditions. Journal of Materials Science. 1981;**16**(9):2419-2433. DOI: 10.1007/BF01113578

[4] Pagnola M, Malmoria M, Barone M, Sirkin H. Analysis of $Fe_{78}Si_9B_{13}$ (% at.) ribbons of noncommercial scrap materials produced by melt spinning equipment. Multidiscipline Modeling in Materials and Structures. 2014;**10**(4):511-524. DOI: 10.1108/MMMS-11-2013-0068

[5] Pagnola M, Barone M, Malmoria M, Sirkin H. Influence of z/w relation in chill block melt spinning (CBMS) process and analysis of thickness in ribbons. Multidiscipline Modeling in Materials and Structures. 2015;**11**(1):23-31. DOI: 10.1108/MMMS-02-2014-0008

[6] Tkatch VI, Limanovski AI, Denisenko SN, Rassolov SG. The effect of the melt-spinning processing parameters on the rate of cooling. Materials Science and Engineering A. 2002; **323**:91-96. DOI: 10.1016/S0921-5093(01)01346-6

[7] Miglierini M. Mossbauer-effect study of the hyperfine field distributions in the residual amorphous phase of Fe-Cu-Nb-Si-B nanocrystalline alloys. Journal of Physics: Condensed Matter. 1994;**6**(7):1431-1438. DOI: 10.1088/0953-8984/6/7/015

[8] Franke H, Dey S, Rosemberg M. Hyperfine fields and local magnetic moments of metallic glasses of 3D-transition metals. Journal of Magnetism and Magnetic Materials. 1980;**15/18**: 1364-1366. DOI: 10.1016/0304-8853(80)90323-6

[9] Busby Y, Pireaux JJ. Metal nanoparticle size distribution in hybrid organic/inorganic films determined by high resolution X-ray photoelectron spectroscopy. Journal of Electron Spectroscopy and Related Phenomena. 2014;**192**:13-18. DOI: 10.1016/j.elspec.2013.12.010

[10] Muraca D, Silveyra J, Pagnola M, Cremaschi M. Nanocrystals magnetic contribution to FINEMET-type soft magnetic materials with Ge addition. Journal of Magnetism and Magnetic Materials. 2009;**321**:3640-3645. DOI: 10.1016/j.jmmm.2009.07.005

[11] Bussmann M, Mostaghimi J, Kirk DW, Graydon JW. A numerical study of steady flow and temperature fields within a melt spinning puddle. International Journal of Heat and Mass Transfer. 2002;**45**:3997-4010. DOI: 10.1016/S0017-9310(02)00112-6

[12] Babei R, Esmaellian H, Varahram N, Davami P. Mathematical and computational modeling of mold filling and heat transfer in metal casting. Iranian Journal of Science & Technology, Transaction B, Engineering. 2005;**29**(B5):511-530. DOI: 10.1.1.573.5964&rep=rep1&type=pdf

[13] Hui XD, Yang YS, Chen XM, Hu ZQ. Transient heat transfer and fluid dynamics during the melt spinning process of $Fe_{78}Si_9B_{12}Mo$ amorphous alloy. Science and Technology of Advanced Materials. 2001;**2**:265-270. DOI: 10.1016/S1468-6996(01)00067-5

[14] Wang GX, Matthys EF. Mathematical simulation of melt flow heat transfer and non-equilibrium solidification in planar flow casting. Modelling and Simulation in Materials Science and Engineering. 2002;**10**:35-55. DOI: 10.1088/0965-0393/10/1/304/pdf

[15] Steen PH, Karcher C. Fluid mechanics of spin casting of metals. Annual Review of Fluid Mechanics. 1997;**29**:373-397. DOI: 10.1146/annurev.fluid.29.1.373

[16] Theisen EA, Davis MJ, Weinstein SJ, Steen PH. Transient behaviour of the planar-flow melt spinning process. Chemical Engineering Science. 2010;**65**:3249-3259. DOI: 10.1016/j.ces.2010.02.018

[17] Sowjanya M, Kishen Kumar Reddy T. Flow dynamics in the melt puddle during planar flow melt spinning process. Materials Today Part A. 2017;**4**(2):3728-3735. DOI: 10.1016/j.matpr.2017.02.268

[18] Sowjanya M, Kishen Kumar Reddy T. Obtaining stable puddle and thinner ribbons during planar flow melt spinning process. Materials Today Part A. 2017;**4**(2):890-897. DOI: 10.1016/j.matpr.2017.01.100

[19] Pagnola M, Malmoria M, Barone M. Biot number behaviour in the chill block melt spinning (CBMS) process. Applied Thermal Engineering. 2016;**103**:807-811. DOI: 10.1016/j.applthermaleng.2016.04.077

[20] Carpenter JK, Steen PH. Heat transfer and solidification in planar-flow melt-spinning: High wheelspeeds. International Journal of Heat and Mass Transfer. 1997;**40**(9):1993-2007. DOI: 10.1016/S0017-9310(96)00305-5

[21] Marrugo AG, Barone M, Useche J, Pagnola M. Experimental investigation of high-speed melt spinning by means of digital image analysis, presented at the Latin America Optics and Photonics Conference; Washington, D.C; 2016. p. LTh2C.5. DOI: 10.1364/LAOP.2016.LTh2C.5

[22] Nigen S, El Kissi N, Piau JM, Sadun S. Velocity field for polymer melts extrusion using particle image velocimetry. Journal of Non-Newtonian Fluid Mechanics. 2003;**112**(2):177-202. DOI: 10.1016/S0377-0257(03)00097-1

[23] Wernet MP, Hadley JA. A high temperature seeding technique for particle image velocimetry. Measurement Science and Technology. 2016;**27**(12):1-10. DOI: 10.1088/0957-0233/27/12/125201/meta

[24] Zhang G, Chanson H. Application of local optical flow methods to high-velocity free-surface flows: Validation and application to stepped chutes. Experimental Thermal and Fluid Science. 2018;**90**:186-199. DOI: 10.1016/j.expthermflusci.2017.09.010

[25] Beauchemin SS, Barron JL. The computation of optical flow. ACM Computing Surveys (CSUR). 1995;**27**(3):433-466. DOI: 10.1145/220000/212141/p433-beauchemin.pdf?

[26] Lucas BD, Kanade T. An iterative image registration technique with an application to stereo vision. In: Proceedings of Imaging Understanding Workshop; 1981. pp. 121-130

[27] Bizjan B, Kuznetsov A, Jeromen A, Govekar E, Sirok B. High-speed camera thermometry of laser droplet generation. Applied Thermal Engineering. 2017;**110**(C):298-305. DOI: 10.1016/j.applthermaleng.2016.08.182

[28] Bizjan B, Širok B, Drnovšek J, Pušnik I. Temperature measurement of mineral melt by means of a high-speed camera. Applied Optics. 2015;**54**(26):7978-7984. DOI: 10.1364/AO.54.007978

IntechOpen